Document Version
Final published version

Citation (APA)
Cambraia Lopes, P., Bauer, J., Salomon, A., Rinaldi, I., Tabacchini, V., Tessonnier, T., Crespo, P., Parodi, K., & Schaart, D. R. (2016). First in situ TOF-PET study using digital photon counters for proton range verification. *Physics in Medicine and Biology*, *61*(16), 6203-6230. https://doi.org/10.1088/0031-9155/61/16/6203

iopscience.iop.org

Home Search Collections Journals About Contact us My IOPscience

First *in situ* TOF-PET study using digital photon counters for proton range verification

This content has been downloaded from IOPscience. Please scroll down to see the full text.

2016 Phys. Med. Biol. 61 6203

(http://iopscience.iop.org/0031-9155/61/16/6203)

View the table of contents for this issue, or go to the journal homepage for more

Download details:

IP Address: 131.180.130.242
This content was downloaded on 26/07/2017 at 15:00

Please note that terms and conditions apply.

You may also be interested in:

Time-resolved imaging of prompt-gamma rays for proton range verification using a knife-edge slit camera based on digital photon counters
Patricia Cambraia Lopes, Enrico Clementel, Paulo Crespo et al.

Beam-on imaging of short-lived positron emitters during proton therapy
H J T Buitenhuis, F Diblen, K W Brzezinski et al.

First full-beam PET acquisitions in proton therapy with a modular dual-head dedicated system
G Sportelli, N Belcari, N Camarlinghi et al.

Evaluation of resistive-plate-chamber-based TOF-PET applied to in-beam particle therapy monitoring
I Torres-Espallardo, F Diblen, H Rohling et al.

Monitoring proton radiation therapy with in-room PET imaging
Xuping Zhu, Samuel España, Juliane Daartz et al.

Initial PET performance evaluation of a preclinical insert for PET/MRI with digital SiPM technology
David Schug, Christoph Lerche, Bjoern Weissler et al.

Full-beam performances of a PET detector with synchrotron therapeutic proton beams
M A Piliero, F Pennazio, M G Bisogni et al.

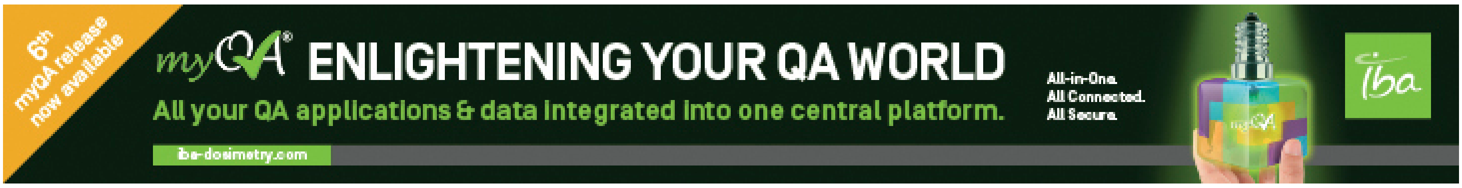
6th myQA release now available
myQA® ENLIGHTENING YOUR QA WORLD
All your QA applications & data integrated into one central platform.
All-in-One. All Connected. All Secure.
iba-dosimetry.com
iba

OPEN ACCESS
IOP Publishing | Institute of Physics and Engineering in Medicine
Physics in Medicine & Biology
Phys. Med. Biol. 61 (2016) 6203–6230
doi:10.1088/0031-9155/61/16/6203

First *in situ* TOF-PET study using digital photon counters for proton range verification

P Cambraia Lopes[1,2,3], **J Bauer**[3,4], **A Salomon**[5], **I Rinaldi**[4,8], **V Tabacchini**[1], **T Tessonnier**[4,7], **P Crespo**[2,6], **K Parodi**[3,7] and **D R Schaart**[1]

[1] Delft University of Technology, Faculty of Applied Sciences, Mekelweg 15, 2629 JB Delft, The Netherlands
[2] Laboratório de Instrumentação e Física Experimental de Partículas, Coimbra, Portugal
[3] Heidelberg Ion-Beam Therapy Center, Heidelberg University Clinic, Heidelberg, Germany
[4] Department of Radiation Oncology, Heidelberg University Clinic, Heidelberg, Germany
[5] Department of Oncology Solutions, Philips Research, Eindhoven, The Netherlands
[6] Physics Department, Universidade de Coimbra, Coimbra, Portugal
[7] Department of Medical Physics, Ludwig Maximilian University, Munich, Germany

E-mail: d.r.schaart@tudelft.nl

Received 14 November 2015, revised 19 April 2016
Accepted for publication 11 May 2016
Published 1 August 2016

Abstract

Positron emission tomography (PET) is the imaging modality most extensively tested for treatment monitoring in particle therapy. Optimal use of PET in proton therapy requires *in situ* acquisition of the relatively strong ^{15}O signal due to its relatively short half-life (~2 min) and high oxygen content in biological tissues, enabling shorter scans that are less sensitive to biological washout. This paper presents the first performance tests of a scaled-down *in situ* time-of-flight (TOF) PET system based on digital photon counters (DPCs) coupled to Cerium-doped Lutetium Yttrium Silicate (LYSO:Ce) crystals, providing quantitative results representative of a dual-head tomograph that complies with spatial constraints typically encountered in clinical practice (2 × 50°, of 360°, transaxial angular acceptance). The proton-induced activity

---

[8] Now at Lyon 1 University and CNRS/IN2P3, UMR 5822, 69622 Villeurbanne, France.

inside polymethylmethacrylate (PMMA) and polyethylene (PE) phantoms was acquired within beam pauses (in-beam) and immediately after irradiation by an actively-delivered synchrotron pencil-beam, with clinically relevant 125.67 MeV/u, 4.6×10^8 protons s^{-1}, and 10^{10} total protons. 3D activity maps reconstructed with and without TOF information are compared to FLUKA simulations, demonstrating the benefit of TOF-PET to reduce limited-angle artefacts using a 382 ps full width at half maximum coincidence resolving time. The time-dependent contributions from different radionuclides to the total count-rate are investigated. We furthermore study the impact of the acquisition time window on the laterally integrated activity depth-profiles, with emphasis on 2 min acquisitions starting at different time points. The results depend on phantom composition and reflect the differences in relative contributions from the radionuclides originating from carbon and oxygen. We observe very good agreement between the shapes of the simulated and measured activity depth-profiles for post-beam protocols. However, our results also suggest that available experimental cross sections underestimate the production of ^{10}C for in-beam acquisitions, which in PE results in an overestimation of the predicted activity range by 1.4 mm. The uncertainty in the activity range measured in PMMA using the DPC-based TOF-PET prototype setup equals 0.2 mm–0.3 mm.

Keywords: positron emission tomography, time-of-flight, proton therapy, in-beam PET, digital photon counters

(Some figures may appear in colour only in the online journal)

1. Introduction

At present, positron emission tomography (PET) is the imaging modality most extensively tested for treatment monitoring during or after irradiation in particle therapy (PT). This technique relies on the coincidence detection of delayed radiation, i.e. pairs of 511 keV annihilation gammas that are emitted in opposite directions as a result of the β^+ decay of irradiation-induced radioactive species produced in the target (by proton and heavy ion beams) and projectiles (heavy ions only). PET has been shown to provide valuable clinical information for quality assurance of the treatment delivery, such as: (1) on the positioning of the irradiated volume, (2) on morphology changes occurring during the course of the fractionated radiotherapy, and, very importantly, (3) on the finite particle range (Nishio *et al* 2006, Parodi *et al* 2007b, Fiedler *et al* 2010, Zhu *et al* 2011, Min *et al* 2013), which in turn is highly sensitive to the factors (1) and (2). These factors may not be sufficiently accounted for at the treatment planning stage or be subject to errors, thus giving rise to considerable range uncertainties (Engelsman *et al* 2013). Despite the rationale for treatment verification towards safer and more effective PT, and despite the clinical evidence of PET as a valuable instrument, it is not yet widely used in daily routine.

One reason for this is the complexity in translating measured activity into delivered dose. So far, the most accurate means for treatment verification has been implemented by comparing the PET activity to predicted activity distributions based on complex and time-consuming Monte Carlo (MC) simulations. Many efforts have been put into this direction, including the implementation into MC of (1) patient models based on computed tomography (CT) (Parodi *et al* 2007a), (2) functional models describing biologic decay (activity clearance/perfusion) (Parodi *et al* 2007b) and (3) experimental cross-section data of the main isotope production channels (Parodi *et al* 2007a, 2008); as well as (1) the fine-tuning of these cross-sections to better match simulated activity to PET measurements (Bauer *et al* 2013), (2) the comparison of different MC interaction models (Seravalli *et al* 2012), (3) development of methods to measure *in vivo* the ^{15}O production and clearance rates from dynamic PET data (Grogg *et al* 2015) and (4) the development of algorithms for automated detection of range deviations to increase the clinical throughput (Helmbrecht *et al* 2012, Frey *et al* 2014).

A main factor limiting the use of PET as a standard PT verification tool is the technological challenge of integrating it at the irradiation site. Optimal use of PET imaging requires the ability to acquire the signal from ^{15}O *in situ*, due to the relatively high abundance of oxygen in biological tissues and its relatively short half-life of ~2 min, requiring shorter scans that are less sensitive to blurring and biological distortion of the induced activity by physiologic mechanisms such as washout, wash-in, and transport. The implementation of a closed-ring PET at the beam nozzle has been argued to be feasible, collision-free with patient table and couch, using two separate heads and retractable arms in a rotating gantry (Kopf *et al* 2004, Crespo 2005). Alternative solutions have been proposed using two rings axially separated or a single ring cut at a slant angle (Tashima *et al* 2012), but all of these implementations cost a larger volume in the patient area and a larger axial field of view (FOV) (Crespo *et al* 2006).

A possible compromise is a dual-head limited-angle tomograph having an opening angle that provides an input port for the therapeutic beam and an escape port for fragments leaving the patient, as well as easier access to the patient (Enghardt *et al* 1999, Nishio *et al* 2006, 2010). In addition, by using flat-panel detectors, the radius (thus, detection efficiency) can be adjusted depending on the irradiation site and spatial constraints (Nishio *et al* 2010). Drawbacks of this approach are the lower (solid angle) detection efficiency, and the presence of image artefacts due to limited-angle tomographic reconstruction (Crespo *et al* 2006). Nevertheless, simulations have shown that image artefacts are significantly reduced in realistic clinical irradiations by including time-of-flight (TOF) information in the reconstruction (Crespo *et al* 2007, Dendooven *et al* 2014). Crespo *et al* (2007) has shown that a coincidence resolving time (CRT) of 200 ps (FWHM) or better is necessary for a dual-head tomograph with a 2 × 134° (of 360°) transaxial angular acceptance. For range estimation, it appears sufficient to have a CRT of 300 ps using a dual-head tomograph with a 2 × 90° (of 360°) transaxial angular acceptance, or 600 ps CRT and a larger, 2 × 120° (of 360°) transaxial angular acceptance (Surti *et al* 2011). In addition to mitigating limited-angle image reconstruction artefacts, TOF information improves the image signal-to-noise ratio on a *per se* poor count-rate scenario, thus representing an important tool in PT PET.

Offline PET (post-therapeutic and outside treatment site, with a 5–10 min delay) has been implemented by means of commercial full-ring PET/CT solutions (Parodi *et al* 2007b, 2012), but have limited clinical applicability (Knopf *et al* 2009) and high impact on patient workflow (long scans). In-room full-ring solutions (nearby irradiation site, with few-minutes delay) were suggested as a good compromise between integration costs and quality (Shakirin *et al* 2011). Efforts have also been put in developing dedicated or custom-made PET tomographs. Examples are the dual-head *in situ* systems (Enghardt *et al* 1999, Iseki *et al* 2003, Nishio *et al* 2006) and in-room full-ring scanners-on-wheels for head-and-neck treatments (Zhu *et al* 2011). Technological developments are ongoing, including those recently reported by Tashima *et al* (2012), Shao *et al* (2014), and Sportelli *et al* (2014).

Here we present the first *in situ* performance test of PET modules based on DPC arrays as the photosensor, i.e. arrays of the digital silicon photomultipliers (dSiPMs) introduced and developed by Philips Digital Photon Counting (PDPC) (Frach *et al* 2009, 2010, Haemisch *et al* 2012). In contrast to the previous works referred to above, we have realized TOF-PET imaging thanks to the fast timing performance of the LYSO:Ce-coupled DPC detectors used (Degenhardt *et al* 2012). SiPMs are solid-state photosensors with high gain and fast time response, which function on the basis of single-photon detection in each of the (typically) several thousand microcells (single photon avalanche photodiodes, SPADs, operated in Geiger-mode), which are connected in parallel in an analog SiPM. Due to the local digitization of the SPAD signals in a digital SiPM (DPC-pixel) (Frach *et al* 2009), the electronic readout noise is much reduced and the sensor response is made even faster in comparison to analog SiPMs (Schaart *et al* 2016). The readout of a dSiPM is relatively simple due to the integration of logic circuitry for photon counting and time-to-digital conversion on the sensor chip, as well as the inclusion of further data acquisition and signal processing capability on the level of the dSiPM array (Frach *et al* 2010, Schaart *et al* 2016). Hence, detectors based on dSiPM arrays are very compact and scalable, making them particularly suitable for large-scale applications (Haemisch *et al* 2012) and applications with high space constraints.

In situ PET may include acquisitions during irradiation (in-beam) and/or after the end of the irradiation (post-beam). A post-beam acquisition with (ideally) zero delay (i.e. starting immediately after the end of irradiation) will be denoted here as an ‘online’ protocol, after (Nishio *et al* 2006). The term ‘in-room’ protocol will be used otherwise, generally referring to post-beam acquisitions with small, few-minute delays. In-beam acquisitions are easier to implement at synchrotron facilities, due to the periodic time-macrostructure of the beam delivery (beam-on/beam-off), allowing for background-free acquisitions (Parodi *et al* 2005a) during the beam pauses (beam-off) in between the spills (beam-on). The so-called ‘in-beam’ PET protocol used in the scope of this work corresponds solely to the case of beam-off in-beam PET. Nevertheless, implementation of in-beam PET during particle extraction at either synchrotron or continuous-wave cyclotron beams is possible with dedicated random suppression techniques that utilize the correlation of the random background structure with the sub-μs-microstructure of the beam (Crespo *et al* 2005). Inclusion of beam-on coincidence data has been shown advantageous and feasible (Crespo *et al* 2005, Parodi *et al* 2008, Sportelli *et al* 2014).

In this work we test a proof-of-concept *in situ* limited-angle PET setup comprising two DPC/LYSO:Ce modules operated in coincidence, under clinically relevant conditions (beam structure, beam current, and irradiation time). In addition, we investigate the influence on the PET reconstruction of different acquisition protocols (mostly based on two-minute acquisition windows with various starting times), focusing especially on the shape of the laterally integrated depth profiles and on the corresponding activity range. To this end, the contributions of the major proton-induced radionuclides to the detected coincidence rate are disentangled and the experimental results are compared to activity simulations using the MC particle transport and interaction code FLUKA (Ferrari *et al* 2005, Böhlen *et al* 2014).

2. Methods and materials

2.1. Experiment description

Figure 1 shows a photograph and a schematic overview of the measurement setup in the experimental room of the Heidelberg Ion-Beam Therapy Center (HIT). Two detectors with a surface area of 66 mm × 66 mm were positioned opposite to each other, such that the distance between the crystal front-surfaces was 121 mm. The setup forms a limited-angle, dual-head TOF-PET tomograph with an absolute transaxial angular acceptance of about 2 × 50° (of 360°, figure 1-bottom), resulting in about 9% relative solid-angle coverage, at the center of the FOV. Thus, the setup has an angular coverage comparable to that of a clinical limited-angle tomograph such as the pioneer BASTEI head scanner at GSI (Crespo *et al* 2006).

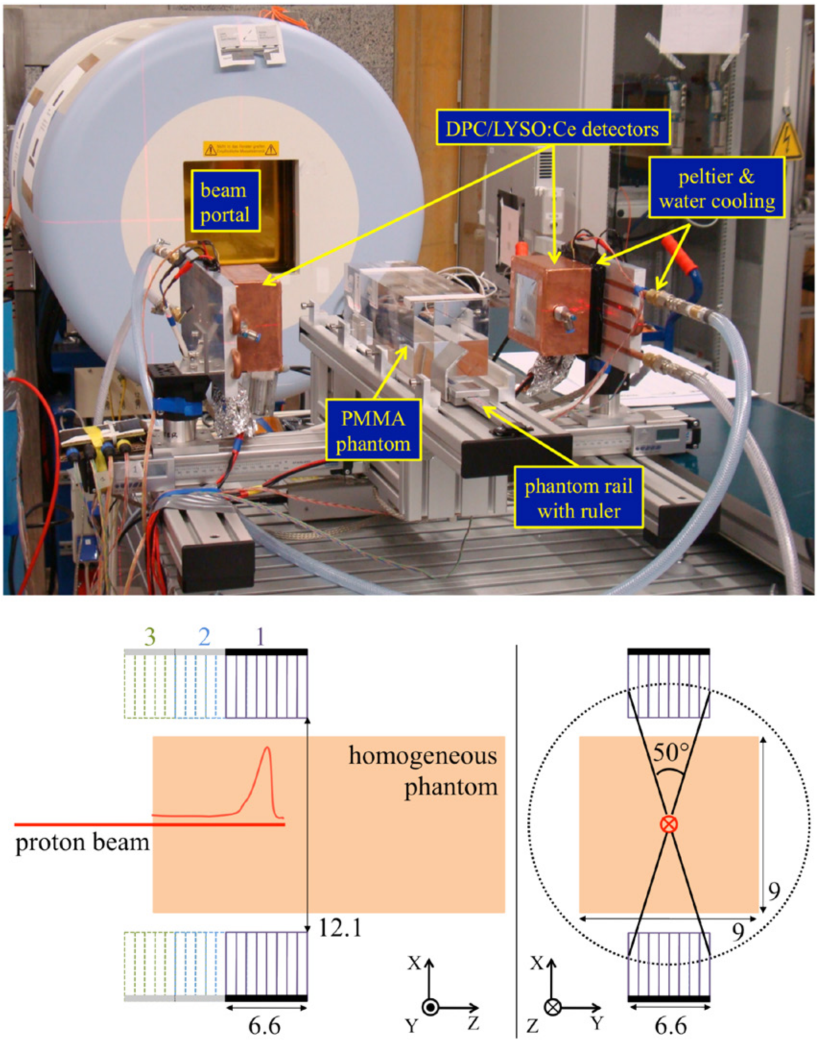

Figure 1. *Top:* photograph of the *in situ* TOF-PET setup at the HIT. The distance between the two detectors in the photograph is larger than in the actual measurement. *Bottom:* schematic overview of the measurement setup (not to scale), with distances displayed in centimeters. Three longitudinal detector positions with FOV overlaps of 2.5 cm covered the full proton beam range. This was accomplished by translating the phantom over its support rail.

Homogeneous phantoms made of polymethylmethacrylate (PMMA, $C_5H_8O_2$, density 1.1845 g cm^{-3}) or polyethylene (PE, C_2H_4, density 0.95 g cm^{-3}) and with dimensions of 9 cm × 9 cm (lateral) and, at least, 30 cm (longitudinal) were irradiated along their longitudinal axis by a proton pencil beam with an energy of 125.67 MeV u^{-1}. The corresponding proton range, defined as the phantom depth at which the dose has decreased to 80% of the maximum value of the depth-dose profile, at the distal side of the Bragg peak, was 9.85 cm in PMMA and 11.69 cm in PE. These values were calculated on the basis of a FLUKA simulation of the depth-dose distribution in water and the water equivalent path lengths of PMMA and PE (viz. 1.165 and 0.982, respectively).

Table 1. Irradiation parameters: beam energy (E), average spill intensity ($\langle I \rangle$), FWHM of the beam focal point at isocenter in air (focus), total number of delivered protons (N_p), total number of beam extractions (spills), average spill duration $\langle t_\mathrm{s} \rangle$, average pause duration $\langle t_\mathrm{p} \rangle$, and total irradiation time $\langle t_\mathrm{irr} \rangle$).

E (MeV/u)	$\langle I \rangle$ (p s^{-1})	Focus (mm)	N_p	Spills	$\langle t_\mathrm{s} \rangle$ (s)	$\langle t_\mathrm{p} \rangle$ (s)	$\langle t_\mathrm{irr} \rangle$ (s)
125.67	4.63×10^8	12.9	1.00×10^{10}	35	0.62	3.80	151

Table 1 summarizes the clinically relevant, synchrotron-delivered irradiation conditions that were used for all the measurements. A total of 10^{10} protons were delivered at an average beam intensity of 4.63×10^8 protons s^{-1} during extractions (spills), which is within the range of a typical single field of a head-and-neck treatment plan (Parodi *et al* 2007b, Bauer *et al* 2014). However, the beam was always pointing at the same spot, coinciding with the long axis of the phantoms, delivering a total dose of about 10 Gy in water at the Bragg peak, calculated considering the width of the beam envelope (focus). The irradiation lasted approximately 2.5 min, including 35 spills intercalated with pauses (table 1). The beam macro structure on average had a period of 4.42 s and a duty cycle (i.e. the spill duration as a percentage of the period) of 14%, which is favorable for realizing in-beam PET measurements during the 34 relatively long irradiation pauses. The relative differences between the mean pause durations of individual irradiations and the average value over all irradiations presented in table 1 were typically below 1%. For the mean spill duration and the total irradiation time these values were 5% and 2%, respectively. Within individual irradiations, the root mean square (RMS) of the pause duration was typically 1%–3% (maximum 4%) of the mean value, while for the spill durations the RMS was 3%–5% of the mean value.

Coincidence data covering the entire proton range in both phantoms were acquired using three different detector positions, as indicated in figure 1-bottom. Detector position ‘1’ was defined as follows: the center of the FOV was aligned with the laser crossing indicating the isocenter. Subsequently, the phantom was positioned such that the center of the detector FOV was located 8 mm proximal to the proton range. Positions ‘2’ and ‘3’ were defined by translating the phantom distally ($+Z$) along the beam direction on its support rail, by 41 mm and 82 mm, respectively, while the detectors were kept at a fixed position. The phantom length that was imaged by two adjacent detector positions corresponded to the total width of about 6 LYSO:Ce crystals (25 mm), so as to avoid areas of near-zero sensitivity when the detectors are operated in coincidence.

To characterize the sensitivity of the PET setup to deviations in the proton range, another series of experiments was performed in which the PMMA phantom was shifted by small increments along the beam axis, relative to position ‘1’, in both the distal ($+Z$) and the proximal ($-Z$) directions. In this way, positron emitter distributions were measured for Bragg peak shifts of -4 mm, -2 mm, -1 mm, 0 mm, 1 mm, and 2 mm. A built-in digital ruler enabled the accurate longitudinal positioning of the phantom on its support rail with an accuracy of ~5 μm.

In all measurements, the activity generated by the protons inside the phantoms was continuously measured during irradiation and during a period of at least 15 min after irradiation. In order to avoid residual phantom activity from previous irradiations, four (PMMA) and three (PE) phantoms of equal dimensions were used alternatingly, allowing the activity in each phantom to decay to negligible levels before using it again.

2.2. Detector description and operation

We used DPC-MO-22–3200 detector modules developed by PDPC, which have been described elsewhere (Degenhardt *et al* 2012, Haemisch *et al* 2012, Schaart *et al* 2016). Each module contains a total of 256 polished $Lu_{1.8}Y_{0.2}SiO_5$:Ce (LYSO:Ce) crystals with dimensions of 3.8 mm × 3.8 mm × 22 mm, covering a total surface area of about 66 mm × 66 mm. The photosensor comprises 2 × 2 DPC3200-22–44 DPC arrays (figure 2-left). Each array is made of 4 × 4 independently read-out DPC chips, each chip comprising 2 × 2 DPC-pixels. The crystals are optically coupled to the DPC-pixels with UV-curable glue (DELO-PHOTOBOND 4436), in a 1:1 arrangement at a 4 mm pitch within each DPC-array, while a small gap (~2 mm) exists in between the DPC-arrays (figure 2-left, Degenhardt *et al* 2012). Each group of 2 × 2 LYSO:Ce crystals is thus coupled to a DPC-chip. These groups are optically isolated from each other by means of reflective foil (Vikuiti Enhanced Specular Reflector (ESR), by 3M), while some light sharing is allowed between crystals on the same DPC chip.

In order to minimize the sensor dark-count rate (DCR), the detectors were cooled using a combination of Peltier elements and a heat exchange plate with internal tap water flow, as in Cambraia Lopes *et al* (2015). The modules were kept inside a light-tight and moisture-free container, continuously flushed by dry nitrogen gas (figure 1-top). The temperature of operation was set as low as practically achievable, ranging from −10 °C to −9 °C for all of the DPC arrays. Cooling reduces sensor dead-time due to dark-count triggers, especially when using low trigger threshold settings (Frach *et al* 2009). The DCR was further reduced by inhibiting the 10% most noisy cells.

The acquisition settings used are within the range of typical values for PET applications (Somlai-Schweiger *et al* 2015): an excess voltage of 2.9 V, an integration time of 165 ns, a validation interval of 10 ns, an 8-OR validation threshold, and a trigger threshold on the 2nd registered photon. The principles of operation of DPCs have already been described and characterized (Frach *et al* 2009, 2010). The programmable thresholds and delays regulate the flow of the acquisition chain and they influence the sensor detection efficiency, gain, and dead time. Briefly, the trigger threshold is the condition necessary to start a validation cycle, which will be followed by an integration period (i.e. photon counting period) if and only if the validation threshold is satisfied during the validation interval. Thresholds are satisfied when a user-defined number of microcells fire in a given logic pattern (Tabacchini *et al* 2014). The trigger logic is implemented on pixel level, whereas the validation, integration, and readout are performed on chip level. Upon readout of a valid event, the DPC-chip outputs the (digital) number of fired cells on each of its four pixels, as well as one time-stamp. The time-stamp is defined as the moment when the trigger threshold is satisfied.

Data acquisition was done in coincidence mode, meaning that the DPC acquisition software made a pre-selection of events to be stored based on their time-stamp values, applying a paralyzable 'cluster window' (i.e. a coincidence window that acts on the level of a detector module) and a non-paralyzable 'coincidence window' between the two detector modules. Both windows were 10 ns long.

All PET acquisitions were synchronized with the beam macrostructure by using the so-called 'spill ON' signal, which reports the irradiation status, yielding a logical true or false depending on whether the beam is on (spill) or off (pause), respectively. This signal served as a trigger to generate a step-like logical signal using a gate/delay generator operating in flip-flop mode, which outputs a signal with a rising edge at the start of the first spill that remains at a logical true thereafter. The gate/delay generator output signal was fed into the DPC electronics as a gate 'enable' signal, such that the PET acquisition started at the same time as the irradiation. The PET measurements were acquired continuously using this configuration. By analyzing the beam record files offline, it was possible to relate the event time-stamps to the corresponding beam status.

Only in-beam data registered during the beam pauses were considered throughout the present work. It should be noted that the relatively high count rate during spills (due to prompt

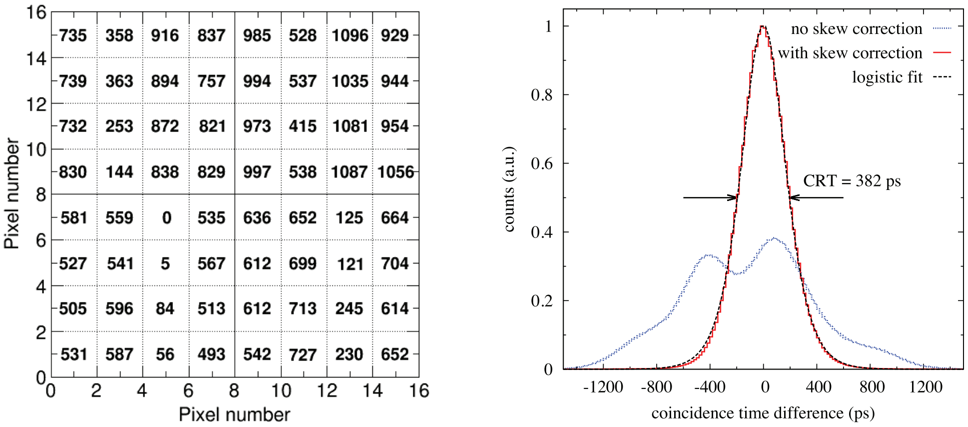

735	358	916	837	985	528	1096	929
739	363	894	757	994	537	1035	944
732	253	872	821	973	415	1081	954
830	144	838	829	997	538	1087	1056
581	559	0	535	636	652	125	664
527	541	5	567	612	699	121	704
505	596	84	513	612	713	245	614
531	587	56	493	542	727	230	652

Figure 2. *Left:* electronic time skews (in picoseconds) of all DPC-chips within a detector module, relative to the chip with the earliest time stamp on average. The module is composed of 2 × 2 arrays of DPC-chips (separated by the solid lines in the figure, which in reality correspond to ~2 mm gaps). All chips (separated by dotted lines) are composed of 2 × 2 pixels. *Right:* coincidence time spectra obtained pre- (dotted line, blue) and post-skew correction (solid line, red), for a total of 3.8 × 10^6 coincidence events, as well as the logistic fit to the latter spectrum (dashed curve, black) obtained from a ^{22}Na point source measurement. The bin width is 20 ps.

gamma rays (Parodi *et al* 2005a)) exceeded the bandwidth of the USB 2.0 interface of the PDPC technology demonstrator kit, which is not designed for high count rates, causing most of the time frames within spills to be dropped. This USB connection transfers the data (prior to coincidence sorting) between the DPC acquisition/control board and the computer.

The in-beam measurement time was about 120 s in total, which corresponded to 80% of the total irradiation time or 93% of the pause time (table 1). The in-beam measurement time did not include the last ~6% time of each pause, due to a small dead time in the beginning of the spills, between the start signal and the actual start of irradiation. It was not considered relevant to correct the acquisition time to include this small (~3% of counts) contribution.

2.3. Offline detector calibration and performance characterization

Time and energy calibrations were implemented offline based on measurements of the 511 keV gamma rays from ^{22}Na point sources with activities of about 0.5 MBq or 0.7 MBq.

2.3.1. Timing. Correcting for electronic time skews between DPC-chips is of utmost importance for obtaining good timing performance. van Dam *et al* (2013) used a direct approach for determining these skews by irradiating the entire DPC-array simultaneously with a pulsed laser. Since this cannot be done after the detector modules have been assembled, we performed time calibration using a practical, indirect approach:

(1) A coincidence measurement was done with the two modules facing each other and the ^{22}Na point source placed just in front of module 1 (M1) (about 1.5 cm away from the crystal front-surfaces) and far enough from module 2 (M2), such that all DPC chips in M2 could detect events in coincidence with M1.
(2) The four central chips of M1, which were closest to the point source, were selected as reference chips, each one from a different DPC-array (note that the center of the detector

front-surface where the point source was located coincides with the crossing between the four sensor arrays, figure 2-left).

(3) For each DPC-array of M2, histograms were created with the time-stamp differences of coincidence events (within the 511 keV photo-peak) recorded between each of its constituting chips and the diametrically opposed reference chip of M1 (a different reference chip on M1 for each array on M2). The histogram peak positions were determined by fitting a logistic curve to each histogram.

(4) As all chips of a certain array on M2 were operated in coincidence with a single reference chip on M1, the time skews between any two M2-chips on the same M2-array (intra-array skews) could be obtained by subtracting the corresponding peak positions calculated in (3).

(5) Steps (1)–(4) were repeated after inverting the roles of M1 and M2, to determine the intra-array time skews of M1.

(6) By selecting coincidences between an (arbitrary) reference M1-chip and each one of the reference M2-chips, the skews between the reference M2-chips can be determined relative to one another as in (4). Thus the skews of all chips within M2 can be determined, relative to an arbitrary M2 chip (and *vice-versa* for M1). The intra-module skews obtained for one of the detector modules are presented in figure 2-left.

(7) Finally, the inter-module skew could be calculated from the peak position of the coincidence time differences between the two modules, obtained in a measurement with a point source placed halfway between the modules.

The skews thus obtained (figure 2-left) are consistent with those reported by van Dam *et al* (2013) within DPC-arrays. Skews of up to 772 ps and 1096 ps were found between chips within an array and within a module, respectively. Figure 2-right shows the coincidence spectrum obtained with a point source, pre- and post-skew correction. The non-corrected spectrum is not only considerably broadened but also distorted and asymmetric, presenting multiple peaks and shoulders. This is attributed to the relatively-high inter-array skews (e.g. the lowest skew of the top-right array in figure 2-left is 415 ps relative to reference chip '0 skew' on the bottom-left array). The logistic distribution function was found to best reproduce the skew-corrected time difference histogram, which is very similar to a Gaussian except that the tails are slightly thicker. The system CRT was 382 ps, consistent with that reported by Degenhardt *et al* (2012) for identical detector modules, taking into account that the CRT degrades by about 100 ps when the 2nd registered photon instead of 1st one is used for triggering (Degenhardt *et al* 2009). In the present work 1st photon triggering was not used to limit the dead time caused by dark-count triggers.

Taking into account the small object size (i.e. the irradiation field) in these experiments, we used a coincidence time window of ±1 ns. Due to the broad coincidence pre-sorting window of 10 ns used by the acquisition software (section 2.2), it was possible to estimate the amount of random coincidences using a 5 ns delayed coincidence window. The random-to-true ratio thus obtained was negligible, i.e. always below 0.5% for in-beam (pauses) and post-beam acquisition protocols (as indicated in figure 9). The cluster window was also shortened in a post-processing step, to ±2 ns.

2.3.2. Energy. Energy calibration was performed using the 511 keV gamma line from a ^{22}Na point source. As in Cambraia Lopes *et al* (2015), the calibration was done on a per-pixel basis, although counts were summed on a per-chip basis to account for light sharing and the fact that the event processing on these sensors is done on chip level. Each chip-event was assigned to the pixel that registered the highest amount of fired cells. The measured number of fired microcells per pixel was corrected for saturation (total of 3200 SPADs per DPC-pixel) by applying a commonly used, logarithmic correction curve (Degenhardt *et al* 2009).

Figure 3 shows energy spectra measured by one of the detector modules. The global energy resolution was 12% (with a per-crystal mean resolution and standard deviation of 10.4% ± 0.7%). No major differences were observed between energy spectra from proton-induced activity acquired in-beam (pauses) and post-beam (post-beam protocols as indicated in figure 9; exemplary 'in-room(b)' protocol is shown in figure 3), except that the in-beam spectra exhibit a small broad pile-up component that peaks at about 0.72 MeV. The scatter fraction was about 22% within the energy window of 450 keV–650 keV, obtained by fitting the proton-induced activity spectra with a Gaussian function (the full-energy peak) plus a linear baseline (the scatter pedestal). Event clustering was performed by summing the energies of multiple chip-events that had time-stamps spaced by less than 2 ns, in order to also detect 511 keV quanta undergoing multiple interactions within the detector. The average number of chips per (cluster) event used for image reconstruction was 1.3 in the energy range from 450 keV to 650 keV.

2.4. Image reconstruction

Image reconstruction was performed using 11 iterations of the maximum-likelihood expectation maximisation (ML-EM) update scheme (Shepp and Vardi 1982):

$$\lambda_j^{(n+1)} = \lambda_j^{(n)} \cdot \frac{\sum_i c_{ij}^{\mathrm{ToF}} \cdot \frac{y_i - \xi_i^{\mathrm{acc}(n)}}{b_i^{(n)}}}{\sum_i c_{ij} a_i} \tag{1}$$

with the estimated non-attenuated activity:

$$b_i^{(n)} = \sum_k c_{ik}^{\mathrm{ToF}} \lambda_k^{(n)}$$

and the estimated attenuation:

$$a_i = \exp\left(-\sum_k l_{ik} \mu_k^{(n)}\right),$$

where y_i is the measured number of coincidences in sinogram entry i and l_{ik} is the interaction length of the line-of-response (LOR) corresponding to sinogram entry i with voxel k. The entries of the system matrix c_{ij}^{TOF} denote the sensitivity of voxel j with respect to sinogram entry i and depend on the TOF information, while μ represents the attenuation coefficients for 511 keV photons and λ the estimated activity per voxel. The estimated number of accidental coincidences (scatter + randoms) is denoted as $\xi_i^{\mathrm{acc}(n)}$ depending on both the estimated activity and the attenuation (details regarding activity reconstruction, scatter, and random correction have been reported by Salomon *et al* (2011)). Each entry of the geometric sensitivity matrix c_{ij} is calculated by the corresponding mean contribution of 128 single lines-of-response distributed between the corresponding crystal pair.

Cubic voxels were used with a side dimension of 1 mm (1/4 of the detector-pixel pitch). For each coincidence event, the crystal with the highest photon count within the chip registering the highest deposited energy was selected for each of the two detectors ('winner-takes-all'). The flat-sinogram back-projection based sensitivity was well estimated over almost the entire FOV. This can be seen from the very good agreement, shown in figure 4-left, between

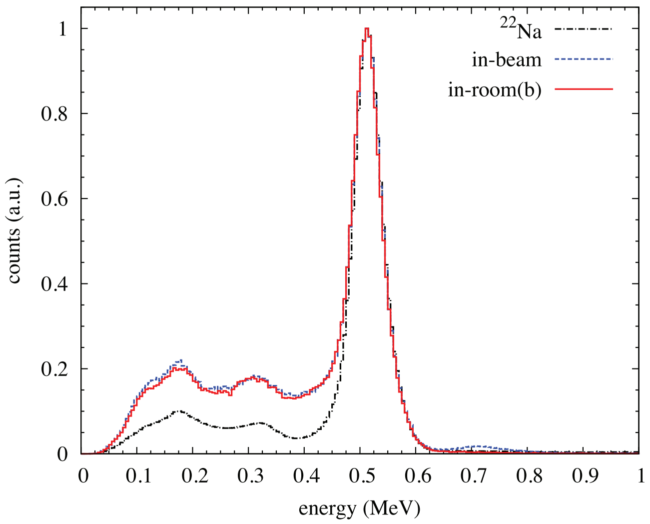

Figure 3. Energy spectra measured in coincidence for a ^{22}Na calibration point source (black curve) and for proton-induced β^+ activity in PMMA during irradiation pauses (2 min duration—'in-beam', blue curve) and after irradiation (2 min delay and 2 min duration—'in-room(b)', red curve). The bin width is 5 keV.

longitudinal profiles obtained with the detector placed at different positions relative to the phantom axis (figure 1-bottom), in the regions where the different FOVs overlap. This is challenging in the present set-up due to the strong acolinearity between LORs and crystal main axis. If TOF information is not used, the agreement at the edges of the FOV is poor (figure 4-right). The reconstructed images and profiles covering the entire proton path that will be presented in the remainder of this work have been merged by doing pixel-by-pixel averaging of the counts in the regions of overlap.

A correction for the efficiency for each crystal was not implemented, so the reconstructed values are regarded as qualitative. The reconstructed images and profiles in this paper are plotted in units of time-averaged counts in order to be comparable to each other.

2.5. Dynamic count-rate modeling

To evaluate the count rate contributions from the main positron emitters, the detected coincidence count-rates were modeled using the mathematical formulation for pulsed beam delivery by Parodi *et al* (2002). The raw coincidence data registered in the energy window of the full-energy peak were analyzed as a function of time, without applying any correction for detection efficiency of the tomograph or in-phantom attenuation of annihilation photons. The modeling was done in two steps.

First, the function describing the exponential decay rates over time was fit to the coincidence rate registered during the 15 min immediately after the end of the irradiation ($t = t_0$), represented in steps of 0.05 s:

$$cps(t > t_0) = \sum_l \lambda_l N_l \,\mathrm{e}^{-\lambda_l (t - t_0)} + C \tag{2}$$

where λ_l is the decay constant of isotope l, and C is a constant accounting for steady background and random coincidences. For PMMA, $l = \{1,\ldots,4\}$ (^{11}C, ^{10}C, ^{15}O, and ^{13}N) and for

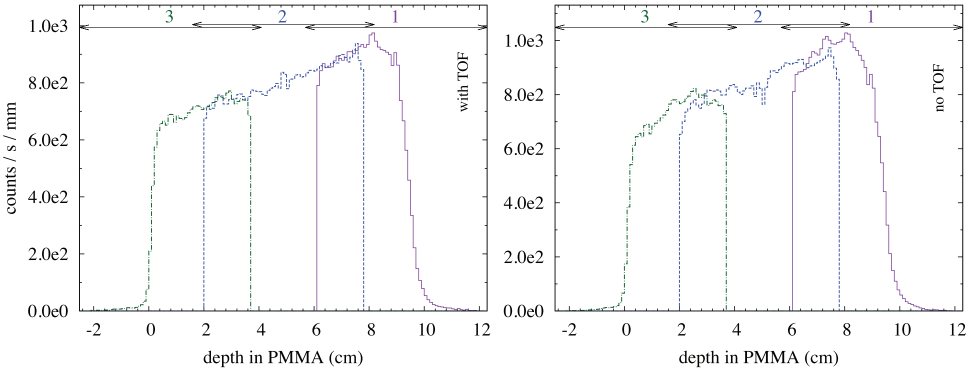

Figure 4. Laterally integrated activity depth-profiles (time-averaged counts) in PMMA, obtained from 15 min measurements starting right after irradiation, with the detectors placed at positions 1, 2, and 3 (figure 1-bottom). Better matching in FOV overlap regions is observed when TOF information is used (left) than in the non-TOF case (right). The last 4 mm (1 crystal) regions at both edges of the FOV were neglected as these had very low counting statistics.

PE, $l = \{1, 2\}$ (^{11}C and ^{10}C). The N_l are fitting parameters which yield the relative amount of isotope species at the end of the irradiation.

In the second step, the relative (or absolute) amount of nuclei of species l present at the start of pause j can be calculated recursively from the corresponding amount present at the start of the previous pause $j-1$, by taking into account the isotope build-up and decay during the previous irradiation cycle. Assuming a constant beam intensity during particle extraction (thus, a constant isotope production rate, P_l), as well as fixed spill duration, t_s, and pause duration, t_p, the count-rate in the beginning of pause j ($cps_{j,l}$) can be calculated from the contributions of all previous cycles by the simple expression (Parodi *et al* 2002):

$$cps_{j,l} = P_l(1 - \mathrm{e}^{-\lambda_l t_s})\left\{\sum_{i=1}^{j} \mathrm{e}^{-\lambda_l (j-i)(t_s+t_p)}\right\}, \quad j = 1, \ldots, 35 \tag{3}$$

where P_l is determined by the fitting parameter, by solving $cps_{35,l} = \lambda_l N_l$. Therefore, the average count rate of isotope l during pause j ('in-beam' $cps_{j,l}$) is given by:

$$\left\langle cps_{j,l} \right\rangle = cps_{j,l} \frac{(1 - \mathrm{e}^{-\lambda_l t_p})}{\lambda_l \cdot t_p} \tag{4}$$

2.6. Calculation of average activity distributions from FLUKA simulations

Simulations of activity distributions were compared to experimental data for the following purposes: (1) to verify the qualitative agreement to the reconstructed activity distributions, obtained post-beam during a long acquisition of 15 min (low noise), in terms of the 2D images and laterally integrated depth profiles (section 3.2); (2) to assess the qualitative agreement to the laterally integrated depth-profiles obtained during short (mostly 2 min long) in-beam and post-beam acquisitions, trying to infer the main causes of discrepancies from the simulated, individual radionuclide contributions to the overall activity profiles (section 3.4); and (3) to compare the predicted activity range (depth in the phantom corresponding to the distal falloff of the longitudinal activity profile) to the ones resulting from fitting the reconstructed depth profiles obtained with different acquisition protocols (section 3.5).

The expected positron-emitter yields were simulated using the MC particle transport and interaction code FLUKA used and further customized at HIT, in its most recent version 2011.2c. This code was found to very well reproduce the amount of proton-induced activity (to within a few percent) and the distal activity range (to within 0.6 mm) measured offline by means of a commercial PET/CT scanner in homogeneous and heterogeneous phantoms, after cross-section tuning of the main reaction channels leading to ^{11}C, ^{15}O, and ^{13}N (Bauer *et al* 2013).

The simulations took into account the phantom composition, proton energy, beam momentum spread, and irradiation time profile used in the experiments. The ionization potentials used for PMMA and PE were 74.8 eV and 57.0 eV, respectively, as in Bauer *et al* (2013), while the cross-sections tuned in that work were also applied. However, in contrast with Bauer *et al* (2013), ^{10}C production is included in the present work. The cross-section data for ^{10}C production from proton interactions on ^{12}C was included in accordance with Parodi *et al* (2008), based on experimental cross-sections described elsewhere (Iljinov *et al* 1991, EXFOR/CSISRS 2007). The number of protons simulated was 5×10^6.

The outcome of the simulations is a spatial distribution of positron-emitter production yields per proton, R_l^{MC}, for each radionuclide species l. In the next step, we calculated the expected spatial distribution of the activity averaged over the PET measurement *duration*, starting with a *delay* since the end of the irradiation ($t_{\mathrm{start}} = t_0 + \mathrm{delay}$), as in (Bauer *et al* 2013):

$$\langle A\rangle_l^{\text{post-beamPET}}(\vec{r}) = A_l(\vec{r};t_0)\mathrm{e}^{-\lambda_l\cdot\mathrm{delay}}\cdot\frac{1-\mathrm{e}^{-\lambda_l\cdot\mathrm{duration}}}{\lambda_l\cdot\mathrm{duration}} \tag{5}$$

where $A_l(\vec{r};t_0)$ is the activity distribution immediately after the last spill. Similar to equation (3), this distribution can be derived by setting $j = 35$, and the isotope production rate as the product of the MC production yields per proton and the average spill intensity:

$$A_l(\vec{r};t_0) \;= \langle I\rangle\cdot R_l^{\mathrm{MC}}(\vec{r})\cdot(1-\mathrm{e}^{-\lambda_l t_s})\left\{\sum_{i=1}^{35}\mathrm{e}^{-\lambda_l(35-i)(t_s+t_p)}\right\} \tag{6}$$

Although a more precise calculation of the activity is possible by using the individual spill intensity and duration values registered in the beam record files, the differences in total activity were found to be negligible due to the stable operation of the synchrotron.

Equation (5) is only valid for a PET acquisition starting after irradiation. The average activity per pause can be calculated in analogy to equation (4) and the average PET activity produced during the whole irradiation can be calculated as the mean value over the total of 34 beam pauses:

$$\langle A\rangle_l^{\text{in-beamPET}}(\vec{r}) = \langle I\rangle\cdot R_l^{\mathrm{MC}}(\vec{r})\frac{(1-\mathrm{e}^{-\lambda_l t_s})(1-\mathrm{e}^{-\lambda_l t_p})}{\lambda_l\cdot t_p}\sum_{j=1}^{34}\left\{\sum_{i=1}^{j}\mathrm{e}^{-\lambda_l(j-i)(t_s+t_p)}\right\}\cdot {}^{1}\!/_{34} \tag{7}$$

Prior to the activity calculation, the simulated spatial distribution of positron-emitter production yields was convoluted with an isotropic Gaussian kernel with a standard deviation of 3.2 mm, as done by Bauer *et al* (2013) for a whole-body scanner, in order to more closely resemble the measured data that is subject to a finite spatial resolution. The voxel size used was 1 mm^3. Although it was impossible to determine the precise value of the spatial resolution of the dual-head PET tomograph on the basis of a single point-source measurement, the Gaussian kernel used seems a reasonable assumption taking into account the crystal size. Although Degenhardt *et al* (2012) reported a spatial resolution of 2.4 mm using identical detector modules mounted on a ring with a crystal-to-crystal distance of 20 cm, the resolution is likely to be worse in the present work due to parallax errors arising from the flat-panel geometry and the small distance between the detector modules.

3. Results and discussion

3.1. Count-rate and DCR measurements

The proton beam intensity of 4.63×10^8 protons s^{-1} was low enough that the transfer rate of events outside de spills (prior to coincidence sorting) between the DPC acquisition/control board and the computer did not exceed the bandwidth bottleneck imposed by the USB 2.0 connection from the PDPC technology demonstrator kit, which constituted the main count rate-limiting factor in our setup (see section 2.2). With the irradiation conditions used (table 1), we registered coincidence count-rates of up to about 8.6 kcps (no energy selection) without losses.

It is to be noted that the DPC sensor in principle can process much higher count-rates. The intrinsic maximum (validated) event rate of the DPC-chip when operated at a 200 MHz clock is 1.3 Mcps, even though in the current DPC-array this is limited to 120 kcps per chip by the available FPGA memory. In our measurements, single validated-event rates of only 1 kcps–1.25 kcps per DPC-chip (averaged over the two detectors and a measurement time of about 15 min since the start of the irradiation) were registered on-chip. An event rate of 1.2 kcps/chip corresponded to 0.9 kcps/chip of single events recorded by the computer. Of these events, 0.04 kcps/chip were selected by the coincidence sorting algorithm. This resulted in a maximum (at the end of the last spill) total recorded coincidence rate of ~5.5 kcps, of which ~1.7 kcps fell within the energy selection window.

The vast majority of the trigger rate was dark-count related and corresponded to events that did not pass the validation threshold (section 2.2). After measuring the DCR per cell on every pixel, the trigger rate can be reduced by disabling the hottest cells on each DPC pixel. In the current experiments we inhibited the 10% noisiest cells, resulting in a DCR of 120 s^{-1}–130 s^{-1} per cell, corresponding to about 75%–80% reduction compared to the case where all cells are active. It should be noted that the DCR measurements were done with the LYSO:Ce crystals coupled to the sensors and that the intrinsic DCR per cell is expected to be about 3 times lower in the absence of the lutetium background.

Trigger rates of ~0.27 Mcps per chip were registered initially (after application of the inhibit map for DCR reduction). We observed a gradual increase by ~0.04 Mcps in every consecutive measurement/irradiation (10^{10} protons) performed on the same day, which could hint at some accumulation of radiation damage. The relative increase was small and dead-time losses were insignificant, as each DPC-chip on average had a 1%–2% occupation time, i.e. the time that the sensor is busy with data acquisition, readout, and recharge (including both non-validated-trigger rates and validated-event rates). After a measurement cycle with a total of 7×10^{10} delivered protons, the DCR was re-measured and we observed an increase in the mean DCR per cell of ~2% and ~5% with and without applying the re-calculated inhibit map, respectively, compared to the initial DCR measurement. These results suggest that regular DCR measurement and inhibit calibration is advisable to maintain detector performance. It should be noted that the detectors were placed quite close to the beam, resulting in higher exposure to neutrons than expected in a realistic *in situ* PET setup. Further studies are required to assess the effect of long-term exposure to secondary radiation on the detector performance.

3.2. High-statistics post-beam PET images and depth-profiles: influence of TOF

To maximize counting statistics, the PET images presented in this section correspond to 15 min long acquisitions, starting immediately after irradiation. The in-beam PET data was excluded so that the results can be compared directly to simulation data tuned to well-calibrated PET measurements performed post-beam with a commercial PET scanner (section 2.6) (Bauer *et al* 2013).

Figure 5 shows orthogonal slices of the 3D PET images obtained in PMMA and PE phantoms. Exemplarily results without and with TOF information are shown for PMMA, in the top and center row, respectively. If TOF information is used, limited-angle artefacts are significantly reduced, although not totally eliminated, as expected (Crespo *et al* 2007, Surti *et al* 2011). These artefacts cause the image to stretch along the X axis, i.e. the axis orthogonal to the detector planes (Crespo *et al* 2006). Even with TOF, the width of the activity distribution in the X direction still is about twice that in the Y direction (figure 5-center-right), while the relative difference in the FWHM of a line profile crossing the center of the beam in the Y direction, between measurement and simulation (the latter is not shown), appears to be only a few percent. The FWHM of the simulated activity in PMMA (not shown) in the same transverse slice as in figure 5-right (Z = phantom depth = 8.0 cm) is 1.5 cm along any direction due to circular symmetry. In case TOF information is not used, the distortion in the X direction is much worse than in the TOF case, while a considerable distortion is observed in the Y direction as well, in the form of a narrowing of the activity width that appears visible in both the sagittal and the transverse views.

In the sagittal slices in figure 5, a slight reduction of intensity can be seen at the Z positions at which the centers of the FOVs corresponding to the different detector positions (figure 1-bottom) are located, viz. at $Z = 0.8$ cm, 4.9 cm, and 9 cm for PMMA, and $Z = 2.65$ cm, 6.75 cm, and 10.85 cm (not visible) for PE. This may be the result of the small gaps (ca. 2 mm = ½ of the crystal pitch) between the 4 sensor arrays in each module (figure 2), in spite of the fact that these were taken into account in the reconstruction. Also noticeable is some intensity increase near the beam entrance position ($Z = 0$), which may be related to an imperfect correction of phantom attenuation. Iterative reconstruction algorithms typically are sensitive to sharp density transitions and because of the very atypical set-up used (e.g. with a very small distance between the phantom and the detectors) these effects are difficult to correct for. No intensity overestimation near the beam entrance position is noticeable in the PE phantom, probably because it is closer to the edge of the FOV (i.e. ~6.5 mm versus 25 mm for PMMA). Interestingly, the phantom-entrance effect is not visible in the sagittal projection images, which are presented in figure 6.

Also shown in figure 6 are the simulated activity distributions projected in the Y direction, while figure 7 shows the laterally integrated depth-profiles. The qualitative agreement between the simulated and measured results is excellent in both figures. On the other hand, the shape of the laterally integrated depth-profiles obtained without TOF information (as shown in figure 4-right for PMMA) is distorted in comparison to the simulated case.

As the CRT of the current setup is not good enough to completely eliminate the limited-angle reconstruction artefacts in the X direction, there is a larger discrepancy between the total number of counts in the simulated and measured sagittal images if slices are considered instead of projection images (~1.2 higher ratio). The qualitative agreement between measurements and simulations thus is considerably better when projections are considered instead of

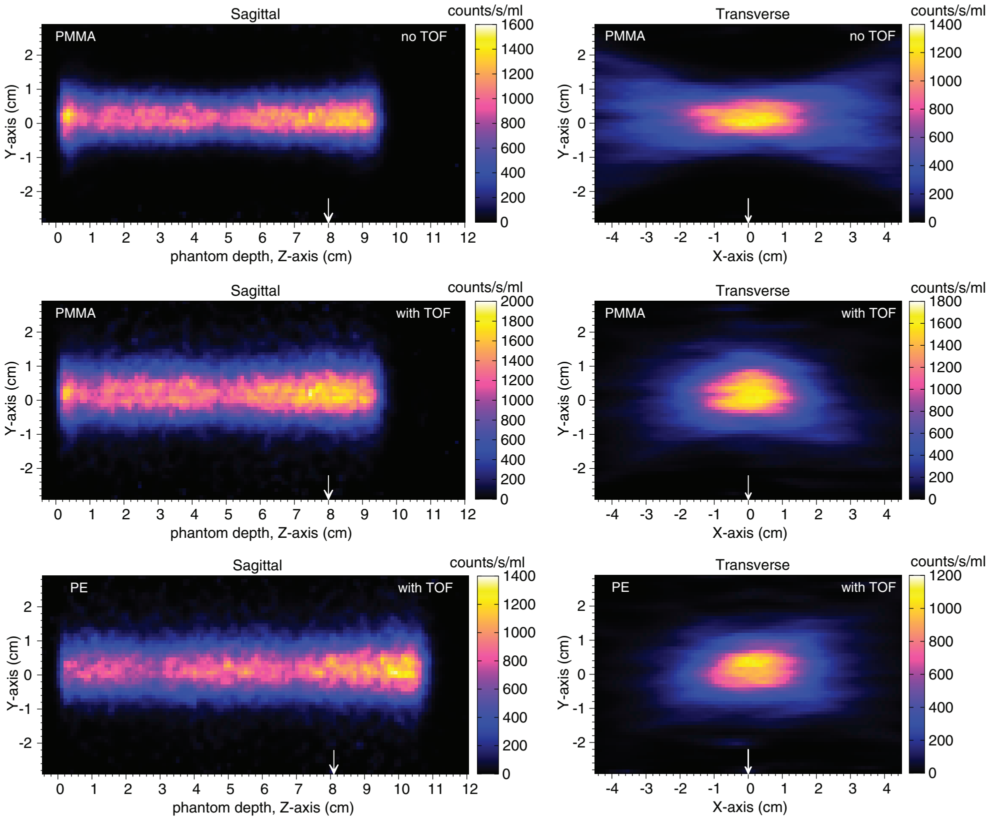

Figure 5. Measured images of proton-induced activity in PMMA, reconstructed without (top) and with (center) TOF information, and in PE (bottom), shown as 2 mm thick sagittal (left) and transverse (right) slices. The white arrows indicate the positions of the orthogonal slices. All images were acquired for 15 min, starting right after irradiation.

slices. The simulated sagittal slices were not shown since they are qualitatively very similar to the corresponding projections presented in figure 6-bottom. For these reasons, only projection images and laterally integrated depth profiles reconstructed with TOF information are considered in the remainder of this work.

3.3. Time-dependent count-rate contributions from major radionuclides

Figure 8 presents the coincidence rate as a function of time, measured for PMMA (top) and PE (bottom) with the detector placed at position 1 (figure 1-bottom). Also shown in figure 8 are the total and radionuclide-specific coincidence rates calculated according to section 2.5. The constant baseline included in the fitting of the post-beam dynamic count-rate yielded a negligible background of about 5 cps, which corroborates with the expected random coincidence rate.

Figure 9 presents the number of detected coincidences for different acquisition time windows. Four of the acquisition protocols considered have a duration of 2 min, with starting times corresponding to the beginning of irradiation (‘in-beam’), the end of irradiation (‘online’), or the end of irradiation plus a delay of 1 min (‘in-room(a)’) or 2 min (‘in-room(b))’. Such ‘in-room’ protocol could represent an *in situ* PET solution, e.g. a dual-head dedicated system

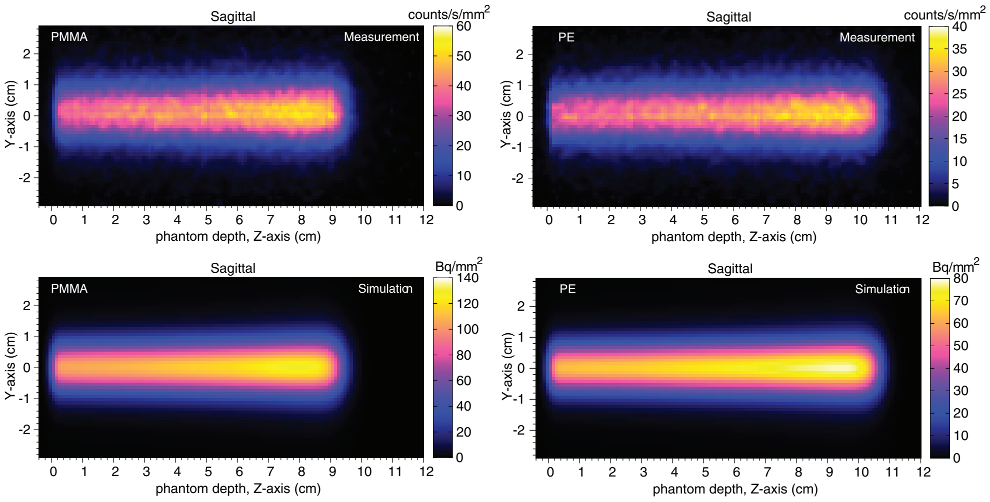

Figure 6. Sagittal views of measured projection images (reconstructed with TOF—top), and corresponding simulations of activity distributions (bottom) in PMMA (left) and PE (right). Images were acquired for 15 min, starting right after irradiation.

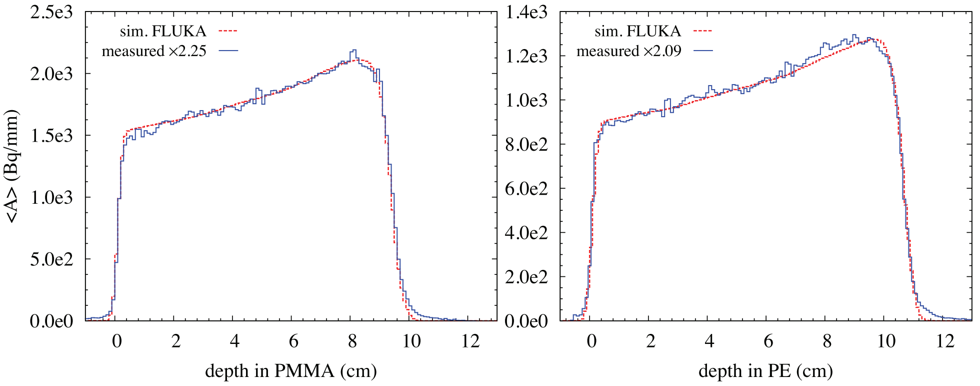

Figure 7. Measured (reconstructed with TOF—blue, solid) and simulated (red, dashed), laterally integrated depth-profiles of proton-induced activity in PMMA (left) and PE (right). All profiles correspond to 15 min acquisitions starting right after irradiation. The measured profiles have been normalized to the same total area as the simulated ones (scale factors are indicated in the legend, while the non-normalized measured profiles have units of counts/s/mm).

that would be kept distant from the irradiation area due to spatial constraints and/or to avoid radiation damage, and would be repositioned on-site after irradiation by robotic arms. For further reference, an ‘in-room(c)’ protocol was considered, having a delay of 2 min and a longer duration of 5 min. This protocol has been found by Min *et al* (2013) to yield results similar to a 20 min PET scan in terms of the average range differences between PET measurements and computed-tomography image-based MC predictions. However, it is to be noted that these authors reported results of clinical trials of much higher complexity, using passive-scattering irradiation fields and a full-ring in-room PET scanner on wheels.

In general, the 2 min *in situ* acquisitions are comparable in terms of the total amount of coincidences detected, with the ‘in-room(b)’ protocol registering the least amount of counts,

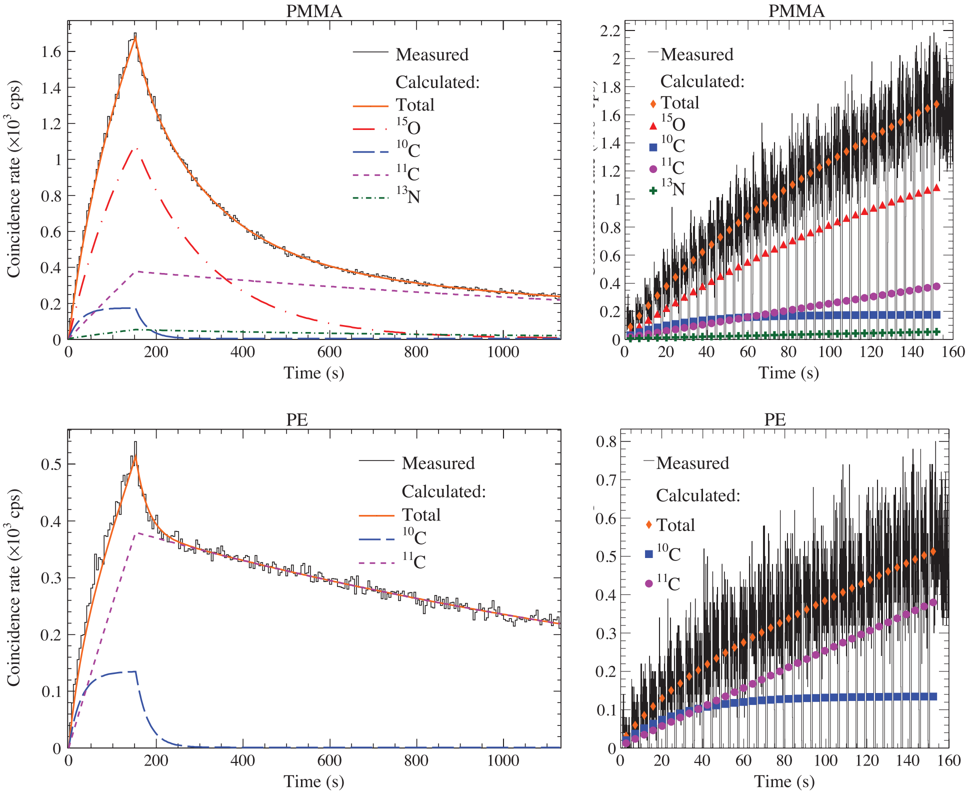

Figure 8. Comparison between measured and modeled coincidence count-rates (post energy selection) for PMMA (top) and PE (bottom). Also shown are the calculated individual contributions from each of the major nuclides. *Left*: measured data is presented with a bin size equal to one irradiation cycle (spill + pause), with each bin centered at the middle of the pause time, and with the count-rate per cycle approximated to the count-rate registered per pause. *Right:* zoom-in of the measured in-beam (pauses) coincidence count-rate, shown with a bin size of 0.05 s, and the model prediction of the average rate per beam pause.

viz. about 37% less than the 'online' case that registered the highest amount. Furthermore, the 'in-room(c)' acquisition registers about 2-times more counts than 'in-room(b)' due to its longer duration (figure 9). Although offline PET imaging is outside the scope of this paper, it is interesting to note that the amount of 43×10^4 registered coincidence counts from PMMA (not shown) for what is considered a best-case 'offline' delay of 5 min and a long scan duration of 30 min (Parodi *et al* 2008), is lower than the amount of 46×10^4 coincidences that would be obtained during the beam pauses and an extra *in situ* time of 7 min (i.e. 'in-beam' + 'online' + 'in-room(c)' protocols), if the detection efficiency is the same in both cases.

The total amount of modeled coincidences agreed with the detected coincidences shown in figure 9, to within <1% for the 'online' and 'in-room(a)–(c)' protocols, indicating the goodness of the fit. The amount of in-beam modeled coincidences summed over all pauses and for all isotopes, using equation (4), yielded ~4% higher amount of counts for PMMA and ~2% lower amount of counts for PE, compared to the detected counts listed in figure 9. It is to be noted that the full pause time was considered in equation (4), corresponding to a total in-beam time of 129 s, instead of the 120 s duration of the 'in-beam' measurement protocol considered,

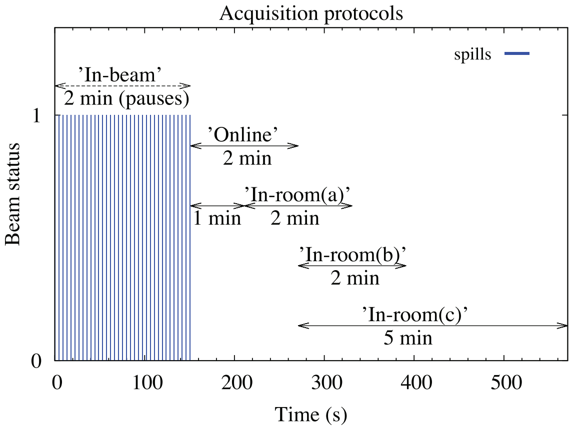

Total coincidences ($\times 10^4$)

PMMA	PE
12.11	3.96
14.96	4.79
11.57	4.30
9.40	4.14
18.76	9.85

Figure 9. Definitions of acquisition protocols (left) and the corresponding measured total numbers of coincidences, post energy selection (displayed in-line on the right), from PMMA and PE phantoms. The coincidence counts were obtained with the detector placed at position 1 (figure 1-bottom). The 'in-beam' PET protocol corresponds to acquisitions during the beam pauses in between spills.

which in turn is expected to yield about 3% less counts compared to a measurement over the total pause time (section 2.2). Nevertheless, the agreement between the modeled and the measured in-beam count rate is satisfactory, as shown in figure 8.

Figure 10 shows the modeled relative amounts of coincidences from each of the main radionuclides produced in PMMA and PE, obtained with the *in situ* protocols, for detector position 1. Counts originating from ^{15}O surpass counts from other nuclides for all *in situ* protocols in PMMA, except for the 'in-room(c)' case in which ^{11}C disintegrations dominate. The fraction of ^{15}O counts for the 'offline' protocol is 8% only (not shown). Counts from ^{10}C, with a short half-life of 19.3 s, are found especially in the 'in-beam' acquisitions.

Changes can be noticed in the relative amount of coincidences from individual nuclides when the detectors are looking at the more proximal parts of the proton path (detector positions 2 and 3 in figure 1-bottom). Figure 11 shows the ratio of coincidences from carbon radionuclides (^{10}C plus ^{11}C) and ^{15}O (C/O ratio) for different detector positions and protocols. The C/O ratio is higher in general for detector positions 2 and 3 than for position 1. The maximum difference is observed for the 'in-beam' protocol, between positions 3 and 1, viz. a relative increase of 1.45. Overall, the C/O values in PMMA range from 0.5 to 1.3, consistent with previous values reported by Parodi *et al* (2005b). If weighted by stoichiometry, the C/O$^{\mathrm{w}}$ ratios range from 20% to 52%. Finally, the amount of ^{13}N counts is relatively low (<7%) in all protocols.

The observed differences between detector positions are expected given the different energy dependency of the production cross-sections: the cross-section for the oxygen production channel, ^{16}O(p,pn)^{15}O, is more peaked and higher for lower proton energies, compared to the main carbon production channel, ^{12}C(p,pn)^{11}C, and the ^{16}O(p,3p3n)^{11}C channel (Bauer *et al* 2013). Therefore, a lower C/O is expected at the distal end of the proton path (position 1) compared to the more proximal phantom depths (positions 2 and 3). Likewise, the energy-dependent cross-section curve for the production channel ^{12}C(p,p2n)^{10}C is considerably shallower and has a lower energy threshold than that of the main channels leading to ^{15}O and ^{11}C (Iljinov *et al* 1991, EXFOR/CSISRS 2007). This may explain the larger differences in C/O ratio between detector position 1 and positions 2 and 3 for the 'in-beam' protocol compared to the other protocols.

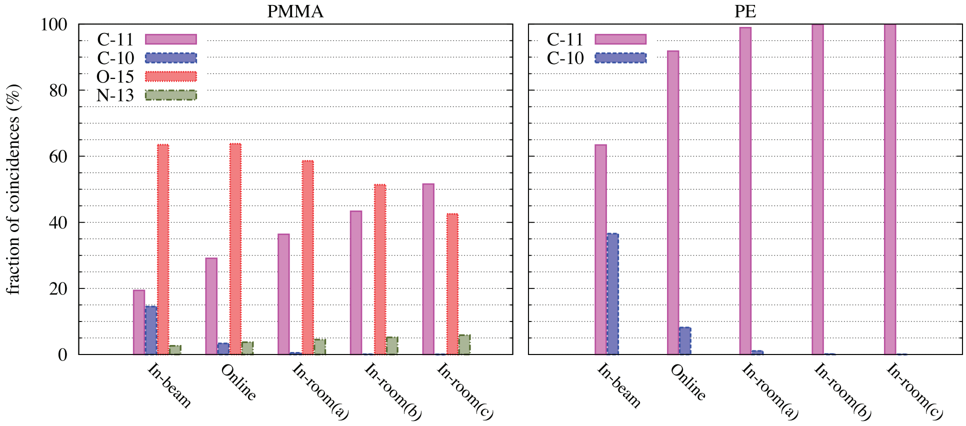

Figure 10. Modeled relative contributions of individual radionuclides to the count rate for PMMA (left) and PE (right), for different acquisition protocols (figure 9), obtained with the detector placed at position 1 (figure 1-bottom).

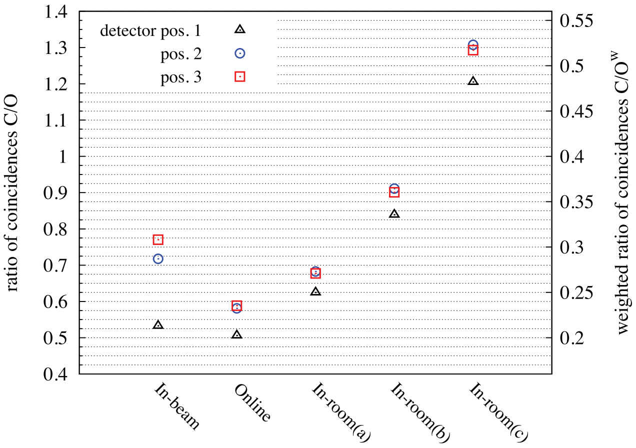

Figure 11. Carbon-to-oxygen (C/O) coincidence ratios in PMMA (modeled according to section 2.5), for different detector positions (figure 1-bottom) and acquisition protocols (figure 9). The carbon coincidences include contributions from ^{11}C and ^{10}C. The right axis displays the ratio of coincidences weighted by relative abundance of target nuclides (C/O^{w}).

3.4. Short PET acquisitions: activity distributions versus time window

Figure 12 shows the PET projection images obtained for the ‘in-beam’, ‘online’, and ‘in-room(b)’ protocols (figure 9). Figure 13-top shows the corresponding laterally integrated depth-profiles. Since protocols ‘in-room(a)–(c)’ yielded qualitatively very similar results, only ‘in-room(b)’ is shown. The results present a hint of the crystal pattern (4 mm pitch), as the reconstruction algorithm becomes more sensitive to the detector discretization when the statistical fluctuations increase, compared to section 3.2.

The largest differences are observed between the ‘in-beam’ and post-beam protocols (both ‘online’ and ‘in-room’), as the ‘in-beam’ depth-profiles are less peaked near the end of the proton range, especially for the PE phantom (figure 13-top). Based on the results of the

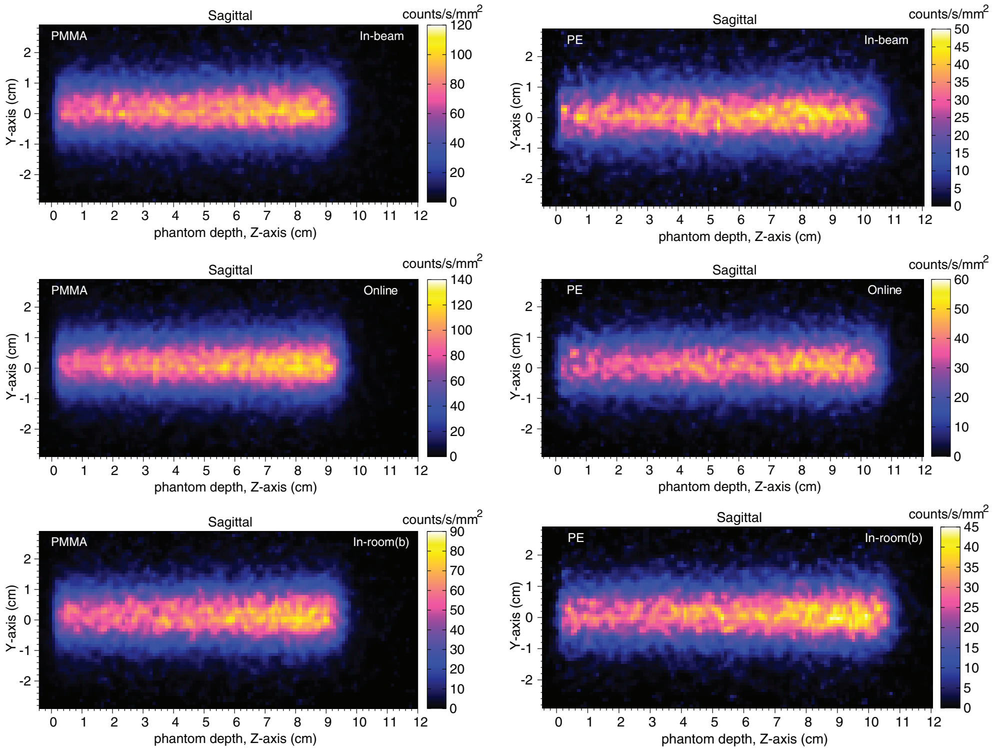

Figure 12. Sagittal views of measured projection images (reconstructed with TOF) of proton-induced activity in PMMA (left) and PE (right), obtained for 2 min long *in situ* PET acquisitions (figure 9).

previous section, these differences are probably due to the higher prevalence of ^{10}C decays (half-life of 19.2 s) in the 'in-beam' protocol (figure 10).

Figure 13 shows the activity depth-profiles simulated with FLUKA (bottom) in comparison to the measured ones (top). The simulated 'in-beam' profiles are shallower than the post-beam ones, especially in PE, in agreement with the measurements. To obtain further insight, the simulated 'in-beam' profiles were split into radionuclide-specific contributions, (figure 14). Indeed, the simulated ^{10}C profile is shallower than the others. Furthermore, due to the absence of ^{15}O activity in PE, the ^{10}C component is more prevalent than in PMMA. Finally, although in PMMA there is additional production of ^{11}C on oxygen, the ^{11}C activity is slightly higher in PE due to the molar ratio of carbon between PE and PMMA of 1.16.

The scale factors that normalize the measured activity depth-profiles to the same area as the simulated ones are not the same for all protocols. These values are presented in table 2. The scale factors appear to be consistent between the 'online' and 'in-room' protocols for PMMA, while for PE they are consistent between the 'in-room' cases. These results indicate that the total predicted activity in PMMA is underestimated by about 9%–10% for the 'in-beam' protocol, while in PE the underestimation is about 18% for the 'in-beam' protocol and a few percent for the 'online' protocol. These differences might be due to an underestimation of the ^{10}C production, resulting from inaccuracies in the corresponding cross-section data. This hypothesis would also be consistent with the observed differences between the shapes of the simulated and measured 'in-beam' profiles in figure 13 (which are not observed for the other protocols).

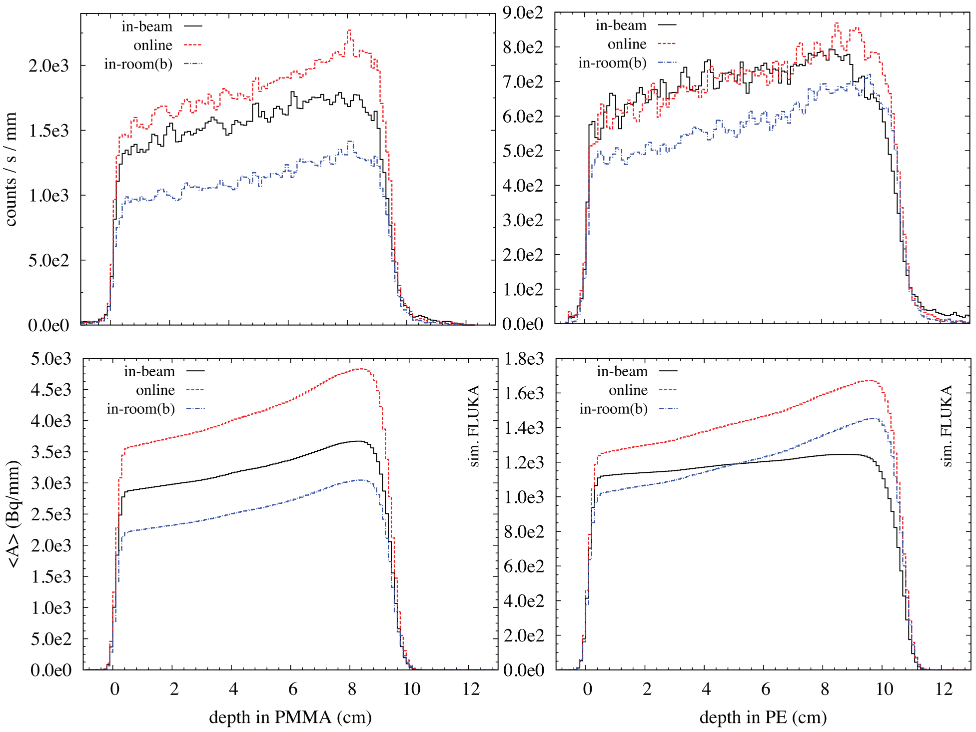

Figure 13. *Top*: laterally integrated measured depth-profiles (reconstructed with TOF) of proton-induced activity in PMMA (left) and PE (right), obtained during 2 min long *in situ* PET acquisitions (figure 9). *Bottom:* corresponding simulated activity depth-profiles. Measured profiles are not calibrated to absolute activity.

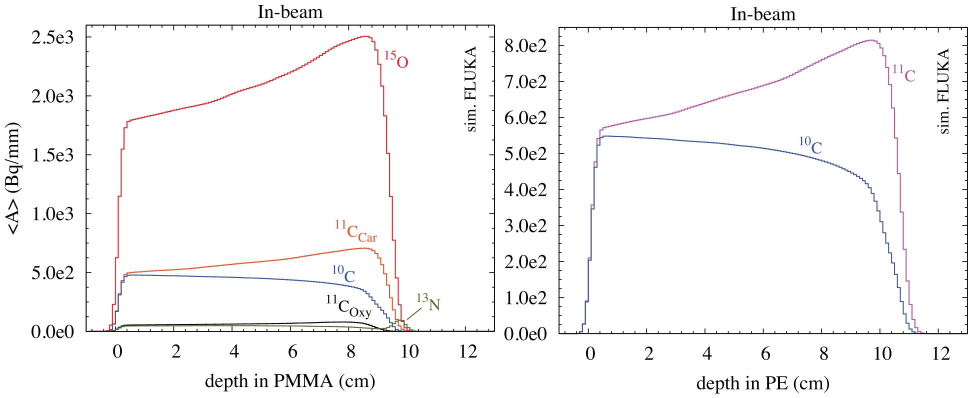

Figure 14. Simulated radionuclide-specific activity depth-profiles obtained during beam pauses, for PMMA (left) and PE (right). The ^{11}C activity is split between the two different production channels, viz. ^{12}C(p,pn)^{11}C (^{11}C$_{\mathrm{Car}}$) and ^{16}O(p,3p3n)^{11}C (^{11}C$_{\mathrm{Oxy}}$).

3.5. Range assessment: precision and bias for short PET acquisitions

The activity range was estimated by fitting a sigmoid curve to the distal end of the laterally integrated activity depth-profiles and determining the z-position (phantom depth) of the

Table 2. Scale factors for normalization of the measured laterally-integrated depth profiles to the same area-under-the-curve as the simulated ones (Norm$_{\text{area}}$).

	Norm$_{\text{area}}$	
	PMMA	PE
In-beam	2.06	1.72
Online	2.27	2.05
In-room(a)	2.29	2.11
In-room(b)	2.29	2.11
In-room(c)	2.27	2.10

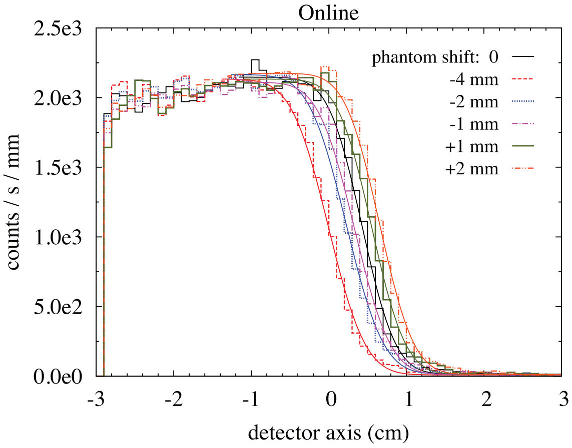

Figure 15. Laterally integrated measured depth-profiles (reconstructed with TOF) of proton-induced activity in PMMA, obtained from 2 min long PET acquisitions, starting right after irradiation, with the phantom positioned such that the center of the FOV was located 8 mm proximal to the proton range (phantom shift = 0) and for various phantom shifts along the beam axis. The smooth curves correspond to sigmoid fits to the data.

inflexion point of the fitted curve. The 50% peak pickoff value is a typical way of determining activity range (e.g. Surti *et al* 2011, Shao *et al* 2014). For this purpose we used the four-parameter complementary error function previously described by Henriquet *et al* (2012). Figure 15 shows some examples obtained with the 'online' protocol.

The uncertainty in determining the activity range in PMMA was estimated as the standard deviation between six samples. Each profile was acquired with the proton range at a different location within the detector FOV, by shifting the phantom over known, small distances along the beam axis. The fitting range was between the profile mean and the distal end of the detector FOV, using a data set corresponding to one detector FOV of about 6 cm length along the beam path (figure 15). Phantom shifts of 1 mm are clearly distinguishable, see figure 15. The uncertainty in the activity range is represented by the error bars on the blue squares in figure 16-left and varies between ±0.2 and ±0.3 mm (one standard deviation).

The blue squares in left- and right-hand plots of figure 16 show the difference (bias) between the activity range and the proton range in PMMA and PE, respectively, where the proton range was determined from simulated depth-dose profiles (section 2.1). The differences between the various protocols are small, with the exception of the 'in-beam' measurement in PE, which differed by 1.6 mm and 1.9 mm relative to the 'online' and 'in-room(c)' protocols, respectively.

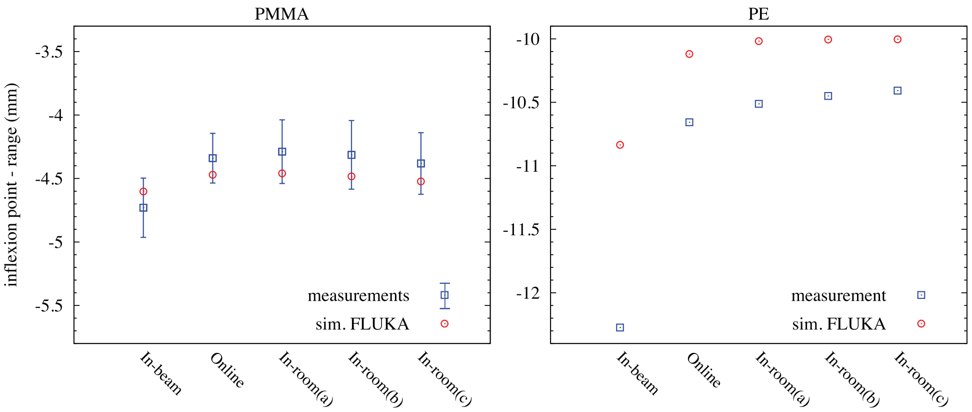

Figure 16. Differences (bias) between estimated activity range (inflexion point from sigmoid fit) and proton range, obtained from experimental (blue squares) and simulated (red circles) data, for PMMA (left) and PE (right). For PMMA, the mean and standard deviation (error bars) of six samples from the experimental data are shown.

The bias in PE is more than 2 times larger than in PMMA for all protocols, which may be due to the absence of counts from ^{15}O and ^{13}N in PE. The energy threshold for the production channel ^{16}O(p,pn)^{15}O is lower than for the channel ^{12}C(p,pn)^{11}C (viz. 16.6 MeV versus 20.3 MeV), yielding a lower proton residual range in PMMA (Parodi *et al* 2000). Moreover, despite the relatively small amount of nitrogen counts, the reaction ^{16}O(p,2p2n)^{13}N has a low threshold of 5.66 MeV (Beebe-Wang *et al* 2003) and the cross-section curve is strongly peaked at low proton energies (Bauer *et al* 2013), leading to a noticeable contribution at the very end of the activity profile in PMMA (figure 14).

The red circles in figure 16 represent the bias between the simulated activity range and proton range. The simulations are found to agree with the experimental results to within 0.2 mm for PMMA and to within 0.5 mm for PE, except for the 'in-beam' protocol in PE for which the discrepancy increases to 1.4 mm. These results corroborate with the findings of section 3.4 regarding a presumable underestimation of ^{10}C counts in the simulation, taking into account that the ^{10}C production energy threshold (viz. 34.5 MeV (Beebe-Wang *et al* 2003)) is considerable lower than those of the other isotopes.

4. Conclusions

We have characterized, for the first time, the performance of TOF-PET detectors based on dSiPMs (viz. digital photon counters—DPCs) for imaging proton-induced β^+ activity *in situ*. PET acquisitions were done within beam pauses (in-beam) and immediately after irradiation of PMMA and PE phantoms by an actively-delivered synchrotron pencil beam, with a clinically relevant energy (125.67 MeV/u), intensity (4.6×10^8 protons s^{-1}), and total number of protons (10^{10}). The *in situ* TOF-PET prototype consisted of two detectors containing DPC arrays coupled in a 1-to-1 arrangement to LYSO:Ce crystal arrays with a 4 mm pitch. Coincidence count-rates of up to 8.6 kcps were registered (using a coincidence window of ±1 ns) while the crystal front-surfaces were placed at ~6 cm from the beam axis, representing a scaled-down version of a limited-angle dual-head PET system (2 × 50°, of 360°, transaxial angular acceptance). With this configuration, the scatter fraction was found to be 22%, while the energy resolution for 511 keV annihilation quanta equaled 12% FWHM and the random-to-true ratio was negligible ($<$0.5%).

Fully 3D TOF-PET image reconstruction yielded distortion-free projection images in the mid-plane between the detectors, as well as laterally integrated depth-profiles of the activity distribution over nearly the entire detector FOV, which compare well with FLUKA simulations. Inspection of beam-transverse image slices reconstructed with and without TOF information demonstrate the benefit of TOF reconstruction for the reduction of limited-angle artefacts, although the full elimination of these artefacts requires a better CRT than the 382 ps FWHM obtained with 2nd-photon triggering in the present setup.

The build-up of the in-beam coincidence rate as well as the post-beam decay were successfully modeled to disentangle the individual contributions from the major radionuclides involved. Differences in their relative contributions are observed at different phantom depths. The maximum variation in the C/O coincidence ratio is found for in-beam acquisitions (viz. C/O is 1.45-times higher when the detector is looking at the phantom-start region compared to the end-of-range region), which is attributed to the contribution from short-lived ^{10}C.

Laterally integrated activity depth-profiles from short (2 min) in-beam and variable-delay post-beam PET acquisitions were compared with each other and with FLUKA simulations. The uncertainty in the activity range determined from sigmoid fits to the measured profiles in PMMA is 0.2 mm–0.3 mm (SD out of six samples, between ~0.1M and ~0.15M crystal pairs reconstructed). Good agreement is observed between the simulated and measured profile shapes, as well as between the simulated and measured activity ranges (up to 0.5 mm difference in PE) for the post-beam protocols. However, a comparison of the areas under the simulated and measured activity curves suggests an underestimation by 9%–10% (PMMA) and 18% (PE) of the total simulated activity in the case of in-beam acquisition. This is supported by the observed overestimation of the simulated activity range by 1.4 mm in PE, which is presumably due to an underestimation of ^{10}C counts in the simulated profiles.

In conclusion, this work provides a first demonstration of the feasibility of using DPC-based detectors for *in situ* TOF-PET imaging for proton therapy monitoring. The results presented are representative of a TOF-PET dual-panel tomograph that would comply with the spatial constraints typically encountered in clinical practice, thus providing information relevant to the development of clinical in-beam TOF-PET systems. Further studies will be necessary to understand the influence of radiation damage on the long-term performance of DPC-based detectors. Finally, our results indicate that further work is required to improve the prediction of proton-induced ^{10}C activity, which is relevant in particular for *in situ* PET systems that aim at measuring the activity in-beam.

Acknowledgments

This work was funded in part by the foundation for Fundamental Research on Matter (FOM), The Netherlands (grant no. 09NIG18), by the European Union Seventh Framework Program (grant agreement no. 241851), by the German Ministry for Education and Research (grant agreement no. 01IB13001G), and by the German Research Foundation DFG (KFO 214). P Cambraia Lopes was supported by grant no. SFRH/BD/73705/2010 and P Crespo by grant no. SFRH/BPD/39223/2007, both from FCT—Fundação para a Ciência e a Tecnologia, Lisbon, Portugal, co-funded by the European Social Fund and by POPH—Programa Operacional Potencial Humano. P Crespo is currently supported by QREN—FEDER under the Sistema de Incentivos à Investigação e Desenvolvimento Tecnológico (CENTRO-07-ST24-FEDER-002007, project 'Radiation for Life').

The authors would like to thank Philips Digital Photon Counting, in particular Carsten Degenhardt, York Haemisch, Ralf Schulze and Ben Zwaans, for fruitful discussions and help with the DPC hardware and software implementations. We acknowledge Jeroen Koning, Kees Langelaan and William van Goozen (DEMO, TU Delft) for technical support with the measurement setup, Stephan Brons (HIT, Heidelberg) for on-site technical support and advice on beam-related specifications, and Jan Huizenga (TU Delft) for support with the data acquisition and control electronics. We also thank Peter Dendooven (KVI, Groningen), Stefan Seifert (TU Delft), and Giacomo Borghi (TU Delft) for helpful discussions.

References

Bauer J *et al* 2014 Integration and evaluation of automated Monte Carlo simulations in the clinical practice of scanned proton and carbon ion beam therapy *Phys. Med. Biol.* **59** 4635–59

Bauer J, Unholtz D, Kurz C and Parodi K 2013 An experimental approach to improve the Monte Carlo modeling of offline PET/CT-imaging of positron emitters induced by scanned proton beams *Phys. Med. Biol.* **58** 5193–213

Beebe-Wang J, Vaska P, Dilmanian F A, Peggs S G and Schlyer D J 2003 Simulation of proton therapy treatment verification via PET imaging of induced positron-emitters *2003 IEEE Nuclear Science Symp. and Medical Imaging Conf. Record* pp 2496–500

Böhlen T T, Cerutti F, Chin M P W, Fassò A, Ferrari A, Ortega P G, Mairani A, Salad P R, Smirnov G and Vlachoudis V 2014 The FLUKA code: developments and challenges for high energy and medical applications *Nucl. Data Sheets* **120** 211–4

Cambraia Lopes P *et al* 2015 Time-resolved imaging of prompt-gamma rays for proton range verification using a knife-edge slit camera based on digital photon counters *Phys. Med. Biol.* **60** 6063–85

Crespo P 2005 Optimization of in-beam positron emission tomography for monitoring heavy ion tumor therapy *PhD Thesis* Technischen Universität Darmstadt

Crespo P, Barthel T, Frais-Kölbl H, Griesmayer E, Heidel K, Parodi K, Pawelke J and Enghardt W 2005 Suppression of random coincidences during in-beam PET measurements at ion beam radiotherapy facilities *IEEE Trans. Nucl. Sci.* **52** 980–7

Crespo P, Shakirin G and Enghardt W 2006 On the detector arrangement for in-beam PET for hadron therapy monitoring *Phys. Med. Biol.* **51** 2143–63

Crespo P, Shakirin G, Fiedler F, Enghardt W and Wagner A 2007 Direct time-of-flight for quantitative, real-time in-beam PET: a concept and feasibility study *Phys. Med. Biol.* **52** 6795–811

Degenhardt C, Prescher G, Frach T, Thon A, de Gruyter R, Schmitz A and Ballizany R 2009 The digital silicon photomultiplier—a novel sensor for the detection of scintillation light *2009 IEEE Nuclear Science Symp. Conf. Record* pp 2383–6

Degenhardt C, Rodrigues P, Trindade A, Zwaans B, Mülhens O, Dorscheid R, Thon A, Salomon A and Frach T 2012 Performance evaluation of a prototype positron emission tomography scanner using digital photon counters (DPC) *2012 IEEE Nuclear Science Symp. and Medical Imaging Conf. Record* pp 2820–4

Dendooven P *et al* 2014 TOF-PET scanner configurations for quality assurance in proton therapy: a patient case study *Radiother. Oncol.* **110** S28–9

Engelsman M, Schwarz M and Dong L 2013 Physics controversies in proton therapy *Semin. Radiat. Oncol.* **23** 88–96

Enghardt W, Debus J, Haberer T, Hasch B G, Hinz R, Jäkel O, Krämer M, Lauckner K and Pawelke J 1999 The application of PET to quality assurance of heavy-ion tumor therapy *Strahlenther. Onkol.* **175** 33–6

EXFOR/CSISRS 2007 Experimental nuclear reaction data www.nndc.bnl.gov/nndc/exfor/ Accessed 28 March 2007

Ferrari A, Sala P R, Fassò A and Ranft J 2005 *FLUKA: a Multi-particle Transport Code* CERN-2005-10, INFN/TC_05/11, SLAC-R-773 Available from: www.fluka.org/fluka.php?id=license&mm2=3

Fiedler F, Shakirin G, Skowron J, Braess H, Crespo P, Kunath D, Pawelke J, Pönisch F and Enghardt W 2010 On the effectiveness of ion range determination from in-beam PET data *Phys. Med. Biol.* **55** 1989–98

Frach Th, Prescher G, Degenhardt C, de Gruyter R, Schmitz A and Ballizany R 2009 The digital silicon photomultiplier—principle of operation and intrinsic detector performance *2009 IEEE Nuclear Science Symp. Conf. Record* pp 1959–65

Frach Th, Prescher G, Degenhardt C and Zwaans B 2010 The digital silicon photomultiplier—system architecture and performance evaluation *2010 IEEE Nuclear Science Symp. Conf. Record* pp 1722–7

Frey K, Unholtz D, Bauer J, Debus J, Min C H, Bortfeld T, Paganetti H and Parodi K 2014 Automation and uncertainty analysis of a method for *in vivo* range verification in particle therapy *Phys. Med. Biol.* **59** 5903–19

Grogg K *et al* 2015 Mapping ^{15}O production rate for proton therapy verification *Int. J. Radiat. Oncol. Biol. Phys.* **92** 453–9

Haemisch Y, Frach Th, Degenhardt C and Thon A 2012 Fully digital arrays of silicon photomultipliers (dSiPM)—a scalable alternative to vacuum photomultiplier tubes (PMT) *Phys. Procedia* **37** 1546–60

Helmbrecht S, Santiago A, Enghardt W, Kuess P and Fiedler F 2012 On the feasibility of automatic detection of range deviations from in-beam PET data *Phys. Med. Biol.* **57** 1387–97

Henriquet P, Testa E, Chevallier M, Dauvergne D, Dedes G, Freud N, Krimmer J, Létang J M, Ray C, Richard M-H and Sauli F 2012 Interaction vertex imaging (IVI) for carbon ion therapy monitoring: a feasibility study *Phys. Med. Biol.* **57** 4655–69

Iljinov A S, Semenov V G, Semenova M P, Sobolevsky N M and Udovenko L V 1991 *Production of Radionuclides at Intermediate Energies* (Berlin: Springer)

Iseki Y *et al* 2003 Positron camera for range verification of heavy-ion radiotherapy *Nucl. Instr. Meth. Phys. Res.* A **515** 840–9

Knopf A, Parodi K, Bortfeld T, Shih H A and Paganetti H 2009 Systematic analysis of biological and physical limitations of proton beam range verification with offline PET/CT scans *Phys. Med. Biol.* **54** 4477–95

Kopf U, Heeg P and Emde P 2004 The gantry irradiation room at the Heidelberg irradiation facility *GSI Rep.* 2004-1 (*Ann. Rep.* 2003) p 183

Min C H, Zhu X, Winey B A, Grogg K, Testa M, Fakhri G E, Bortfeld T R, Paganetti H and Shih H A 2013 Clinical application of in-room positron emission tomography for *in vivo* treatment monitoring in proton radiation therapy *Int. J. Radiat. Oncol. Biol. Phys.* **86** 183–9

Nishio T, Miyatake A, Ogino T, Nakagawa K, Saijo N and Esumi H 2010 The development and clinical use of a beam on-line PET system mounted on a rotating gantry port in proton therapy *Int. J. Radiat. Oncol. Biol. Phys.* **76** 277–86

Nishio T, Ogino T, Nomura K and Uchida H 2006 Dose-volume delivery guided proton therapy using beam on-line PET system *Med. Phys.* **33** 4190–7

Parodi K 2012 PET monitoring of hadrontherapy *Nucl. Med. Rev.* **15** (Suppl. C) C37–42

Parodi K, Bortfeld T and Haberer T 2008 Comparison between in-beam and offline positron emission tomography imaging of proton and carbon ion therapeutic irradiation at synchrotron- and cyclotron-based facilities *Int. J. Radiat. Oncol. Biol. Phys.* **71** 945–56

Parodi K, Crespo P, Eickhoff H, Haberer T, Pawelke J, Schardt D and Enghardt W 2005a Random coincidences during in-beam PET measurements at microbunched therapeutic ion beams *Nucl. Instr. Meth. Phys. Res.* A **545** 446–58

Parodi K and Enghardt W 2000 Potential application of PET in quality assurance of proton therapy *Phys. Med. Biol.* **45** N151–6

Parodi K, Enghardt W and Haberer T 2002 In-beam PET measurements of β^+-radioactivity induced by proton beams *Phys. Med. Biol.* **47** 21–36

Parodi K, Ferrari A, Sommerer F and Paganetti H 2007a Clinical CT-based calculations of dose and positron emitter distributions in proton therapy using the FLUKA Monte Carlo code *Phys. Med. Biol.* **52** 3369–87

Parodi K, Paganetti H, Shih H A, Michaud S, Loeffler J S, DeLaney T F, Liebsch N J, Munzenrider J E, Fischman A J, Knopf A and Bortfeld T 2007b Patient study of *in vivo* verification of beam delivery and range, using positron emission tomography and computed tomography imaging after proton therapy *Int. J. Radiat. Oncol. Biol. Phys.* **68** 920–34

Parodi K, Pönisch F and Enghardt W 2005b Experimental study on the feasibility of in-beam PET for accurate monitoring of proton therapy *IEEE Trans. Nuc. Sci.* **52** 778–86

Salomon A, Goedicke A, Schweizer B, Aach T and Schulz V 2011 Simultaneous reconstruction of activity and attenuation for PET/MR *IEEE Trans. Med. Imaging* **30** 804–13

Schaart D R, Charbon E, Frach T and Schulz V 2016 Advances in digital SiPMs and their application in biomedical imaging *Nucl. Instrum. Methods Phys. Res.* A **809** 31–52

Seravalli E, Robert C, Bauer J, Stichelbaut F, Kurz C, Smeets J, Van Ngoc Ty C, Schaart D R, Buvat I, Parodi K and Verhaegen F 2012 Monte Carlo calculations of positron emitter yields in proton radiotherapy *Phys. Med. Biol.* **57** 1659–73

Shakirin G, Braess H, Fiedler F, Kunath D, Laube K, Parodi K, Priegnitz M and Enghardt W 2011 Implementation and workflow for PET monitoring of therapeutic ion irradiation: a comparison of in-beam, in-room, and off-line techniques *Phys. Med. Biol.* **56** 1281–98

Shao Y, Sun X, Lou K, Zhu X R, Mirkovic D, Poenisch F and Grosshans D 2014 In-beam PET imaging for on-line adaptive proton therapy: an initial phantom study *Phys. Med. Biol.* **59** 3373–88

Shepp L A and Vardi Y 1982 Maximum likelihood reconstruction for emission tomography *IEEE Trans. Med. Imaging* **1** 113–22

Somlai-Schweiger I, Schneider F R and Ziegler S I 2015 Performance analysis of digital silicon photomultipliers for PET *J. Instrum.* **10** P05005

Sportelli G *et al* 2014 First full-beam PET acquisitions in proton therapy with a modular dual-head dedicated system *Phys. Med. Biol.* **59** 43–60

Surti S, Zou W, Daube-Witherspoon M E, McDonough J and Karp J S 2011 Design study of an *in situ* PET scanner for use in proton beam therapy *Phys. Med. Biol.* **56** 2667–85

Tabacchini V, Westerwoudt V, Borghi G, Seifert S and Schaart D R 2014 Probabilities of triggering and validation in a digital silicon photomultiplier *J. Instrum.* **9** P06016

Tashima H, Yamaya T, Yoshida E, Kinouchi S, Watanabe M and Tanaka E 2012 A single-ring OpenPET enabling PET imaging during radiotherapy *Phys. Med. Biol.* **57** 4705–18

van Dam H T, Borghi G, Seifert S and Schaart D R 2013 Sub-200 ps CRT in monolithic scintillator PET detectors using digital SiPM arrays and maximum likelihood interaction time estimation *Phys. Med. Biol.* **58** 3243–57

Zhu X, España S, Daartz J, Liebsch N, Ouyang J, Paganetti H, Bortfeld T R and El Fakhri G 2011 Monitoring proton radiation therapy with in-room PET imaging *Phys. Med. Biol.* **56** 4041–57